npj | quantum materials

Article

Published in partnership with Nanjing University

https://doi.org/10.1038/s41535-025-00816-w

Three-dimensional nature of anomalous Hall conductivity in $YMn_6Sn_{6-x}Ga_x$, $x \approx 0.55$

Hari Bhandari[1,2,3] ✉, Zhenhua Ning[4], Po-Hao Chang[3,5], Peter E. Siegfried[3,5], Resham B. Regmi[1,2], Mohamed El. Gazzah[1,2], Albert V. Davydov[6], Allen G. Oliver[7], Liqin Ke[4,8], Igor I. Mazin[3,5] & Nirmal J. Ghimire[1,2] ✉

The unique geometry of kagome lattices leads to topological features such as flat bands and Dirac cones. When paired with ferromagnetism and a Fermi level near Dirac points, they offer a platform for realizing topological Chern magnetotransport. This prospect recently drew interest in the ferrimagnetic kagome metal $TbMn_6Sn_6$. However, density functional theory (DFT) calculations indicate that its 2D Chern gap lies well above the Fermi energy, raising questions about its role in anomalous Hall conductivity. Here, we study $YMn_6Sn_{5.45}Ga_{0.55}$, a structurally and electronically similar material, and find that its intrinsic anomalous Hall effect is three-dimensional. This demonstrates that the Hall response in such compounds does not originate from 2D Chern gaps. Additionally, we confirm that the newly proposed empirical scaling relation for extrinsic Hall conductivity is universally governed by spin fluctuations.

Kagome lattice magnets have attracted significant interest in condensed matter physics due to their high frustration in the case of antiferromagnetic interactions. Over the past decade, this interest has grown, as it has been shown that even unfrustrated ferromagnetic (or nonmagnetic) kagome planes can exhibit nontrivial electronic features, such as flat bands and Dirac cones[1–7]. Recently, particular attention has been directed toward the so-called 166 family, the RMn_6Sn_6 compounds, where R represents a rare-earth element[8–16]. In these compounds, Mn atoms form kagome planes, and the crystal structure provides a diverse material space for manipulating both electronic and magnetic properties (Fig. 1). Compounds with non-magnetic R atoms are simpler because magnetism arises solely from the Mn sublattice; however, they are also more complex due to frustrated interplanar magnetic interactions. As shown in Fig. 1, although all Mn planes are crystallographically equivalent, the exchange interactions are not; there are two distinct exchange paths: one (J_1) across the Sn layer and the other (J_2) across the RSn layer. In YMn_6Sn_6 (Y166), a R166 compound with non-magnetic R atom, $J_2 > 0$ (i.e., antiferromagnetic), while the dominant interaction is $J_1 < 0$. As in most metals, the exchange coupling decays relatively slowly with distance (roughly as $1/d^3$), so the minimal model Hamiltonian includes J_1, J_2, and J_3. Notably, this Hamiltonian is frustrated if $J_2J_3 < 0$, resulting in intriguing spin-spiral orders that exhibit phenomena such as the topological Hall effect[17,18] and Lifshitz transitions[19].

Replacing Y with a magnetic ion that strongly couples to the neighboring Mn planes introduces an additional indirect ferromagnetic coupling between these planes, which can overcome the direct antiferromagnetic J_2 and remove magnetic frustration. This occurs in Tb166[15,20–25] and is now well understood[12,16]. Additionally, due to well-understood reasons[16], Tb has an easy axis anisotropy along the crystallographic c direction, making the material a collinear easy-axis ferrimagnet at low temperatures, leading to the observation of the anamolous Hall effect (AHE) (in contrast to Y166, which is an easy-plane spiral antiferromagnet). Er166 lies close to the critical boundary between collinear and noncollinear ordering due to thermal fluctations of Er magnetic moments[26]. Because of these specific characteristics, Tb166 recently garnered significant interest for various different properties[12,20,22–24,27,28], including a putative two-dimensional (2D) Chern gap around 130 meV above the Fermi energy, as inferred from scanning tunneling measurements[20]. One of the consequences of a 2D Chern gap, when close to the Fermi energy, is large anomalous Hall effect. The intrinsic contribution to the anomalous Hall effect extracted from the scaling of the anomalous Hall resistivity matches the value expected from the Chern gap around 130 meV above the Fermi energy[20]. However, density functional

[1]Department of Physics and Astronomy, University of Notre Dame, Notre Dame, IN, 46556, USA. [2]Stravropoulos Center for Complex Quantum Matter, University of Notre Dame, Notre Dame, IN, 46556, USA. [3]Department of Physics and Astronomy, George Mason University, Fairfax, VA, 22030, USA. [4]Ames National Laboratory, U.S. Department of Energy, Ames, Iowa, 50011, USA. [5]Quantum Science and Engineering Center, George Mason University, Fairfax, VA, 22030, USA. [6]Materials Science and Engineering Division, National Institute of Standards and Technology (NIST), Gaithersburg, Maryland, 20899, USA. [7]Department of Chemistry and Biochemistry, University of Notre Dame, Notre Dame, IN, 46556, USA. [8]Department of Materials Science and Engineering, University of Virginia, Charlottesville, VA 22904, USA.
✉e-mail: hbhandar@gmu.edu; nghimire@nd.edu

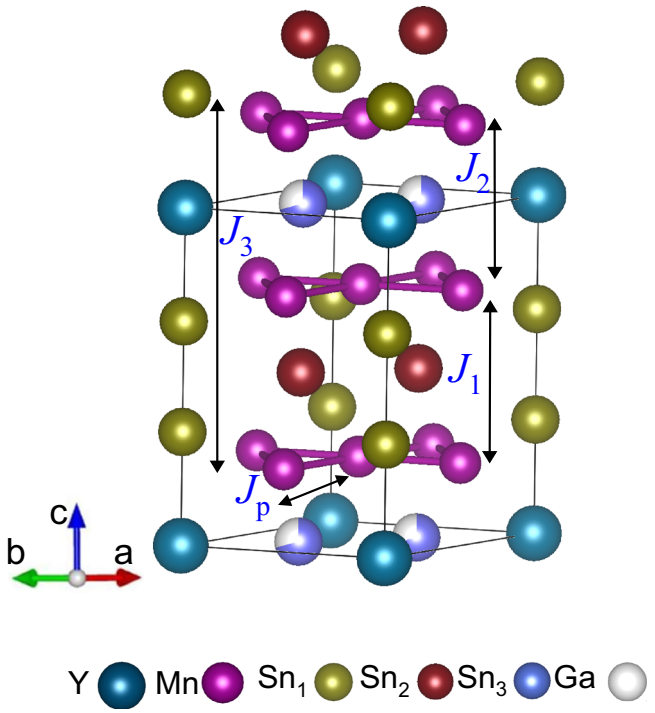

Fig. 1 | Crystal structure. Sketch of the crystal structure of $YMn_6Sn_{5.45}Ga_{0.55}$. J_is ($i = 1, 2, 3$) represent the exchange constants and J_p represents the in-plane exchange constant.

calculations[12,16,29] consistently have shown that the 2D-Chern gap in Tb166 lies about 700 meV above the Fermi energy and does not contribute to the anomalous Hall conductivity (AHC). Instead, this AHC arises from several different regions in the Brillouin zone in ferrimagnetic Tb166[12]. Additionally, an empirical scaling relation in the latter study suggested a potential contribution of spin fluctuations to the extrinsic anomalous Hall conductivity, an effect not previously investigated.

Regarding the latter, the standard method based on the theory by Crépieux and Bruno[30] for extracting the intrinsic (related to the Berry phases of conducting electron) and extrinsic (due to electron scattering) contributions to the AHC is to fit the temperature dependence of the AHC to a simple scaling relation,

$$\sigma_{xy} = a\sigma_{xx}^2 + c \quad (1)$$

where $c = \sigma_{xy}^A$ represents the intrinsic AHC, while the first term arises from defect scattering. This scaling relation has been widely used to extract the intrinsic AHC in various materials[4,20,31]. However, Crépieux and Bruno's derivation did not account for scattering from thermally excited spin fluctuations, and currently a theoretical analysis of the effect of spin fluctuations on AHC is lacking.

Analyzing the Tb166 data, we found[12] that Eq. (1) poorly describes σ_{xy} at higher temperatures, where scattering from spin fluctuations becomes increasingly important. At the same time, we found that the most fluctuating species in Tb166 is Tb, which fluctuates more strongly than Mn. We also found that the empirical formula,

$$\sigma_{xy} = a\sigma_{xx}^2 + d/\sigma_{xx} + c, \quad (2)$$

fits the experimental data exceptionally well (note that the additional contribution becomes significant when σ_{xx} is small, i.e., at higher temperatures). We tentatively attributed this term to spin fluctuations, primarily from Tb.

The role of magnons in extrinsic AHC was discussed by Yang et al.[32]. In particular, they argue that magnon scattering follows what they called "universality class C", where the skew scattering can be neglected (albeit this is in contradiction, for instance with refs. 33,34 and side jump contribution is a universal constant. While this paper makes a number of of model assumptions (such as treating magnons in the "itinerant-s/localized-s model", while our system is itinerant and the same electrons that ensure magnetism also carry transport), and its final formulas cannot be directly applied to experiment, their conclusions are qualitatively useful for us: they introduce a model parameter ξ, chracterizing the relative strength of the magnon scattering, and show that AHC is increasing with this parameter, if it is sufficiently large. This is qualitatively the same behavior as in our empirical formula, Eq. (2), where this additional increase at high temperatures is absorbed in the d/σ_{xx} term. It is worth noting that the possibility that magnon scattering may be important for AHC has been brought up, previously, for instance in ref. 35.

A reliable protocol for extracting AHC from the experiment is crucial. The existing methods[30,31,36] overlook spin fluctuations, and therefore rely on low-temperature data. An equation that accurately describes the AHC across the entire temperature range is of significant practical importance.

In this study, we address two key aspects concerning Tb166: first, whether the intrinsic contribution to the AHC is linked to the 2D Chern gap, and second, whether the component in the AHC scaling relation, attributed to spin fluctuations, can be observed in another *R*166 compound that does not contain Tb. This is particularly relevant as Tb was thought to be crucial for both the Chern-gap induced AHE[20] and the enhancement of spin fluctuations[12].

An ideal compound to investigate these properties would be a *R*166 compound with a non-magnetic *R* atom and a soft, and relatively isotropic ferromagnet. Such a compound would allow the access to the saturated ferromagnetic state in a standard laboratory setting, enabling measurements of anomalous Hall resistivity over a broad temperature range and in both in-plane and out-of-plane directions. We found that $YMn_6Sn_{6-x}Ga_x$, $0.30 \le x \le 0.61$ meet these criteria[37] and selected one particular composition $YMn_6Sn_{5.45}Ga_{0.55}$ for the study. Our results show that the intrinsic AHC in this compound is comparable to that in Tb166 for the out-of-plane magnetic field (B), where the Chern gap is expected to contribute to the AHC. At the same time, we observed a similar AHC in the in-plane B, where the Chern gap contribution is not expected, confirming the 3D nature of the AHC. Furthermore, we verified the new AHC scaling introduced in ref. 12 and confirmed its spin-fluctuational origin.

Results and discussion

Crystallography

The crystal structure and atomic composition of $YMn_6Sn_{5.45}Ga_{0.55}$ (Y166-Ga) were determined using single crystal X-ray diffraction. Similar to the parent compound YMn_6Sn_6 (Y166), Y166-Ga adopts a hexagonal *P6/mmm* structure ($a = b = 5.4784$ Å, $c = 8.925$ Å), consisting of kagome planes [Mn_3Sn] separated by two inequivalent layers Sn_2 and Sn_3YGa, as illustrated in Fig. 1.

The structure exhibits Sn-site doping with Ga, specifically at the Sn3 site (Wyckoff position 2c). This was confirmed through modeling efforts for partial Ga occupancy at other Sn sites, which either resulted in poorer fits to the data or nonsensical Ga occupancy values. Refinement analysis determined the Sn:Ga site occupancy to be 0.725:0.175, corresponding to the full chemical formula noted above, i.e., ~0.55 Ga atoms per unit cell. Detailed crystallographic parameters from the single crystal X-ray diffraction experiment are summarized in Table 1.

Our DFT calculations, presented in Section "First principles calculations", also reveal a significant energy advantage for Ga substitution at the Sn3 site in the [Sn_3Y] layer, rather than in the [Mn_3Sn] or [Sn_2] layers. $YMn_6Sn_{5.45}Ga_{0.55}$ can thus be viewed as a moderately hole-doped (≈0.09 h/Mn) derivative of the parent compound Y166.

Magnetic properties

The temperature dependence of magnetic susceptibility ($\chi = M/B$) measured with a magnetic field $B = \mu_0 H$ of 0.1 T parallel to [100] (χ_{100}) and along [001] (χ_{001}) is shown in Fig. 2a. These susceptibility data indicate that Y166-Ga undergoes a paramagnetic-to-ferromagnetic ordering below 350 K, consistent with previous reports[37,38]. Additionally, the easy-plane behavior is

evident from the significantly larger χ_{100} compared to χ_{001} below the transition temperature (T_c), with an anisotropy ratio of $\chi_{100}/\chi_{001} = 5$ just below T_c. It is to be noted that parent compound Y166 orders with a commensurate antiferromagnetic helical structure below 345 K and exhibits an incommensurate double helical structure (DH) upon further cooling[17,19,39], while $YMn_6Sn_{1-x}Ga_x$ compounds show a ferromagnetic transition for doping concentrations $x > 0.30$[37].

Figure 2b, c shows the isothermal magnetization curves of Y166-Ga at some representative temperatures for B||[100] (M_{100}) and [001] (M_{001}), respectively. In the entire temperature range measured M_{100} saturates below 0.5 T with a negligible hysteresis, while M_{001} saturates at slightly larger B. At 1.8 K M_{001} saturates at 2.2 T, which decreases with increasing temperature (1.7 T at 300 K), also with negligibly small hysteresis. At 1.8 K, saturation magnetization (M_{sat}) along [100] is 9.85 μ_B/f.u. while it is 10.7 μ_B/f.u along [001]. In either direction, M_{sat} gradually decreases with the increase in temperature, which attains a value of 7.5 μ_B/f.u. along [100] and 7.7 μ_B/f.u along [001] at 300 K. The ratio of the saturated magnetization at 1.8–300 K ($M_{sat,1.8K}/M_{sat,300K}$) is 1.39 along the [001] direction and 1.31 along the [100] direction. For Tb166, the Mn moment shows the ratio of ~1.05 and the Tb moment exhibits the ratio of around 1.66[12,40]. This suggests that the Mn moments in Y166-Ga experience more fluctuation between 1.8 and 300 K than in Tb166, where the Tb moments are the most fluctuating ones[12]. This observation is consistent with the expectation, as the Curie temperature of Tb166 is about 70 K higher than that of Y166-Ga.

Table 1 | Crystallographic data, atomic coordinates and equivalent displacement parameters for $YMn_6Sn_{5.45}Ga_{0.55}$

Crystal system				Hexagonal	
Space group				*P*6/mmm	
Temperature (K)				120(2)	
Wavelength (Å)				0.71073	
Z formula units				1	
$2\theta_{min}$				4.564°	
$2\theta_{max}$				61.206°	
Formula weight (g/mol)				1103.76	
a,b (Å)				5.4784(16)	
c (Å)				8.925(4)	
Volume (Å)^3				231.97(17)	
Density (calculated) (g/cm^3)				7.901	
μ (MoK_α) mm^{-1}				29.896	
Goodness-of-fit on F^2				1.186	
Final *R* indices [I≥2σ (*I*)]				$R_1 = 0.0172$	
				$wR_2 = 0.0392$	
R indices (all data)				$R_1 = 0.0183$	
				$wR_2 = 0.0397$	
Largest diff. peak & hole, e (Å^{-3})				1.128 and −1.341	
Atom	**Wyck**	***x***	***y***	**z**	**Ueq Å²**
Y	1a	1.00000	1.00000	0.00000	0.007(1)
Sn(1)	2e	1.00000	1.00000	0.33674(8)	0.004(1)
Sn(2)	2d	0.33333	0.66667	0.50000	0.006(1)
Sn(3)	2c	0.66667	0.33333	0.000000	0.005(1)
Ga(1)	2c	0.6667	0.33333	0.000000	0.005(1)
Mn(1)	6i	0.50000	0.50000	0.24504(9)	0.005(1)

First principles calculations

To understand the doping-induced phase transition, we adopt the J_1–J_3 effective model proposed in ref. 41. The spin Hamiltonian is expressed as follows

$$H = \sum_{\langle ij \rangle_1} J_1 S_i S_j + \sum_{\langle ij \rangle_2} J_2 S_i S_j + \sum_{\langle ij \rangle_3} J_3 S_i S_j \quad (3)$$

where J_i (i = 1–3) are the exchange interaction parameters as indicated in Fig. 1. The parameters were extracted using the least squared fitting of our DFT calculations into Eq. (3).

According to a thorough DFT-based analysis of the phase diagram for parent Y166 discussed in our earlier work[17], we observed that $U = 0.6$ best reproduce the magnetic states for parent Y166 observed in the experiments. Therefore, in our study, we considered the same U parameter with one additional larger $U = 2$ for comparison.

The results along with those of Y166, taken from ref. 17, are summarized in Table 2. The fitting is achieved with excellent quality in all three cases, as all the relative energy differences between different magnetic states can be consistently and accurately reproduced by the model, especially in the case of $U = 0.6$ where the average error is less than 1 meV. This suggests that the minimal model adopted here is appropriate and reliable.

In Table 2, one can see that while J_1 and J_2 consistently favor ferromagnetic alignment regardless of different U values, the Hubbard U correction tends to stabilize the FM states further as J_3 shifts from positive to negative as U increases. According to the analytically determined phase diagram ref. 41, the spin model for all three U values yields the same correct FM ground state.

To assess the doping effect, we compare the results of the two compounds for the same $U = 0.6$ (i.e., columns 3 and 5). In Y166, J_1 dominates and has the same (opposite) sign as J_3 (J_2). This arrangement leads to a competition between J_2 and J_3 which results in the formation of a helical magnetic state[17,41]. However, with Ga-doping, J_2 becomes ferromagnetic and now comparable to J_1 in strength. Although J_3 becomes antiferromagnetic, it is too weak to induce frustration.

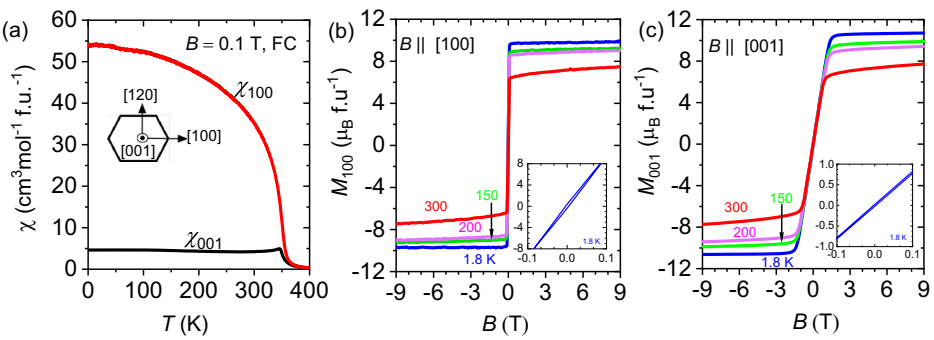

Fig. 2 | Magnetic properties of $YMn_6Sn_{5.45}Ga_{0.55}$. **a** Magnetic susceptibility measured under an external magnetic field B of 0.1 T along the [100] and [001] directions using the field-cooled (FC) protocol. **b**, **c** Magnetization as a function of magnetic field B||[100] (**b**) and B||[001] (**c**) at selected temperatures ranging from 1.8 to 300 K. The insets in panels **b** and **c** show a magnified view of M vs B between ±0.1 T at 1.8 K, revealing the presence of a very small hysteresis loop.

This qualitative shift aligns with expectations, considering the direct alteration of exchange pathways for J_2 and J_3 induced by the presence of doped-Ga. As a consequence of these changes, the frustration that was initially developed in the pure Y166 to promote the helical magnetic state is effectively mitigated. The system undergoes a transition, and the magnetic state collapses into a ferromagnetic (FM) order.

In addition to non-relativistic calculation producing Eq. (3), we performed separate calculations including SOC in order to address magnetic anisotropy (both single-ion and exchange anisotropies). Interestingly, while the calculated ground state is always ferromagnetic, regardless of the value of U, only $U = 2$ gives the correct easy-xy plane anisotropy and $U = 0$ and 0.6 give very small easy-z axis anisotropy.

Electrical resistivity and conductivity

The temperature dependence of electrical resistivity of Y166-Ga, measured with the electric current applied along the [100] direction (ρ_{100}, blue curve) and the [001] direction (ρ_{001}, red curve) over the temperature range 1.8–400 K, is shown in Fig. 3a. The resistivity decreases as temperature decreases, indicating the metallic behavior of the sample. Residual resistivity ratio (RRR), calculated as $\rho(400K)/\rho(2K)$, is 9 for I||[100] and is 18 for I||[001]. These values are smaller than those in Y166[17,19], likely due to disorder induced by doping. Both ρ_{100} and ρ_{001} exhibit a kink at 350 K, indicative of the onset of a ferromagnetic transition, as observed in the susceptibility measurements [Fig. 2a]. Across the entire temperature range, ρ_{100} is greater than ρ_{001}. The conductivity anisotropy, $\sigma_{[001]}/\sigma_{[100]}$, is plotted in Fig. 3b, showing a value >2, which suggests that the electronic transport in Y166-Ga is three dimensional, albeit moderately anisotropic. This behavior differs from that of the parent compound Y166, where the in-plane conductivity is greater than the out-of-plane conductivity[19]. The enhanced c-axis conductivity observed in Y166-Ga is similar to that found in Ge doped YMn_6Sn_6[10].

The anisotropic transport behavior was further investigated by measuring the angular-dependent magnetoresistance (AMR). In this measurement, an electric current I was applied along the [100] direction, while the sample was rotated around the magnetic field within the crystallographic bc-plane, with $I \perp B$ held constant so that only transverse MR was measured. In this configuration, at $\theta = 0°(90°)$, B||[120]([001]). Since the largest magnetic saturation field is below 2.5 T (see Fig. 2), the 9 T magnetic field aligns the magnetic moment M perpendicular to I at all times.

The AMR, defined as $[\{\rho_{xx}(\theta) - \rho_{xx}(\theta = 0)\}/\rho_{xx}(\theta = 0)] \times 100$, measured at 5 K is shown in Fig. 3c, with maximum value of −5.6%, indicating a substantial effect. To gain further insight into this large AMR, we compared the AMR with the ab initio calculated AMR using the GGA + U method. For this purpose, we used the all-electron WIEN2k package[42], varying $U_{\text{eff}} = U - J$ from 1.2 to 2 eV. Assuming an isotropic transport scattering rate, the longitudinal conductivity $\sigma_{xx} \propto \omega_{pl}^2 \propto \sum_{\mathbf{k}} \delta(E - E_{\mathbf{k}}) v_{\mathbf{k}x}^2$, where v is the Fermi velocity. We calculated this quantity using the $19 \times 19 \times 11$ zone-centered k-point mesh and tetrahedron numerical integration, and an otherwise default setup. We found (Fig. 4) that AMR is very sensitive to correlation effects. The best agreement with the experiment occurs at $U_{\text{eff}} = 1.3$ eV, yielding a calculated value of 1.6%, which is over three times smaller than the experimental result but remains the same order of magnitude. This discrepancy may indicate the presence of an anisotropic scattering rate, or an underestimation of spin–orbit coupling (SOC) in the calculation, potentially related to the known underestimation of the AHC in $TbMn_6Sn_6$[12,29].

Anomalous Hall effect

Hall resistivity measured with with B||[001] and the current I||[100] (ρ_{xy}) at representative temperatures is shown in Fig. 5a. The zero-field value of ρ_{xy} corresponds to the anomalous Hall resistivity ρ_{xy}^A. In Fig. 5b, we show the longitudinal conductivity, $\sigma_{xx} = 1/\rho_{xx}$, and the absolute value of the anomalous Hall conductivity, $(|\sigma_{xy}^A|) = -\rho_{xy}/\rho_{xx}$ (valid when $\rho_{yx} \ll \rho_{xx}^2$, and $\rho_{xx} = \rho_{yy}$), as a function of temperature between 1.8 and 300 K. This clearly indicates that $|\sigma_{xy}^A|$ varies with temperature across the entire temperature range. The scaling of the $|\sigma_{xy}^A|$, using the relation presented in Eq. (2), is shown in Fig. 5c. This scaling law effectively fits the high-temperature data, yielding the coefficients a, d, and c, as presented in Table 3 and compared to those from Tb166. The coefficient a, representing impurity scattering, is about an order of magnitude larger in Y166-Ga compared to Tb166, as expected due to increased disorder scattering in the doped sample. The intrinsic anomalous Hall conductivity of Y166-Ga (121 S/cm or 0.14 e^2/h per Mn layer) is comparable to that of Tb166 (140 S/cm). Interestingly, the magnitude of d is smaller in the Y166-Ga than in Tb166, consistent with the hypothesis that the term d/σ_{xx} in Eq. (2) is due to spin fluctuations[12]. Notably, $d \neq 0$ in Y166-Ga despite the absence of highly fluctuating Tb atoms, likely because, as discussed in Section "Magnetic properties", Mn in Y166-Ga fluctuates significantly more than in Tb166. This implies that the d/σ_{xx} is essential in the anomalous Hall scaling of RMn_6Sn_6 compounds due to the presence of Mermin–Wagner fluctuations[17] involving either Mn or R atoms.

The similar magnitude of intrinsic AHC in Y166-Ga and Tb166 suggests that the intrinsic AHC in R166 compounds is a general property of ferrimagnetism rather than a result of exotic Chern physics, consistent with

Table 2 | Calculated exchange couplings J_1, J_2 and J_3 in unit of meV

	$x = 1$			$x = 0$ (Y166)
U	0	0.6	2	0.6
J_1	−14.5	−11.9	−17.3	−12.86
J_2	−21.7	−10.6	−21.9	4.66
J_3	1.8	1.5	−4.0	−2.20

The data for Y166 are taken from ref. 17.

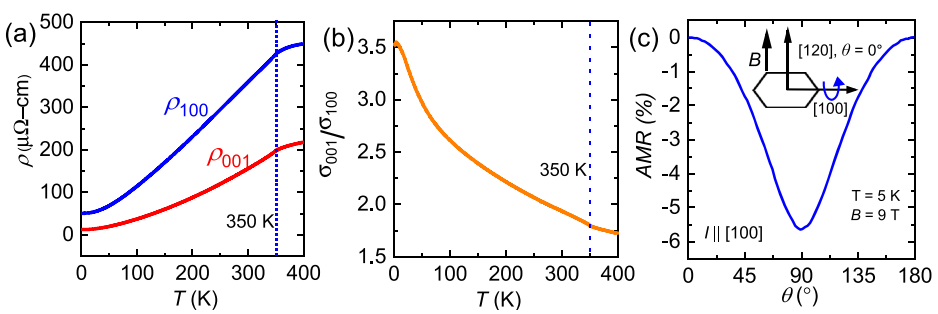

Fig. 3 | Electrical transport properties of $YMn_6Sn_{5.45}Ga_{0.55}$. **a** Electrical resistivity as a function of temperature for current applied along the [100] and [001] directions. **b** Ratio of the conductivity along the [001] direction to that along [100]. **c** Angular magnetoresistance (AMR) as a function of angle θ, measured under a 9 T magnetic field, where the current (I) is along the [100] direction and θ is the angle between the magnetic field and [120] direction, as illustrated by the sketch in panel (**c**).

the conclusions drawn by Jones et al.[12]. This interpretation is further supported by photoemission spectroscopy data from the parent compound Y166[43], which shows no such topological feature above the Fermi energy, with Ga doping shifting the Fermi energy even lower.

To further validate this interpretation, we measured the Hall conductivity of Y166-Ga by applying an in-plane magnetic field, ensuring that any 2D Chern gap contributions would be excluded if present. While measuring this in-plane configuration for Tb166 would require an exceptionally high magnetic field due to magnetic saturation constraints at low temperatures[12,44], Y166-Ga can be measured under standard lab conditions. For consistency with the ρ_{yx} measurement in Fig. 5, we applied the current along the [100] direction and applied the in-plane field along [120]. The Hall resistivity, ρ_{zx}, measured across a range of temperatures from 1.8 to 300 K, is shown in Fig. 6a.

In Fig. 6b, we plot $\sigma_{xx} = 1/\rho_{xx}$ alongside the absolute value of the anomalous Hall conductivity, $\sigma_{zx} = -\rho_{zx}/(\rho_{xx}\rho_{zz})$, which is valid when $\rho_{zx} \ll \rho_{xx}$ and ρ_{zz}. The scaling of σ_{zx}, following the relation in Eq. (2), is presented in Fig. 6c, with the fitting coefficients a, d, and c presented in Table 3. Notably, the intrinsic AHC contribution, represented by coefficient c ($\sigma^A_{zx,int}$), is significantly larger than $\sigma^A_{yx,int}$, indicating that the AHC in Y166-Ga has a 3D nature and can be large without invoking the Chern physics. The coefficient $|d|$ is also larger in this measurement geometry, potentially pointing to enhanced spin-fluctuations, though this cannot be directly compared to Tb166 due to differing Hall geometries and remains a topic of future work on R166 compounds. However, it is noteworthy that the d/σ_{xx} term is also necessary in this case. Nevertheless, our findings reveal that the AHC in Y166-Ga displays 3D characteristics and supports theoretical calculations that suggest the AHC arises from predominantly 3D bands[12], as further discussed in Section "Intrinsic AHC calculations for $TbMn_6Sn_6$ and YMn_6Sn_6".

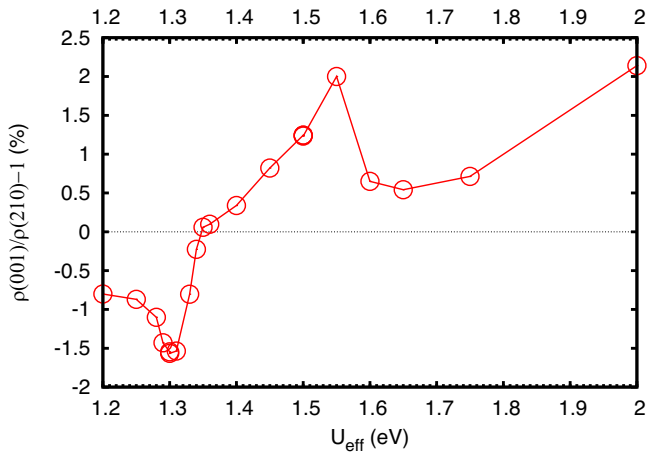

Fig. 4 | Calculated angular magnetoresistance. Angular magnetoresistance between the full polarization along the crystallographic [001] and [120] axes, as a function of the effective Hubbard interaction, calculated for YMn_6Sn_5Ga.

Intrinsic AHC calculations for $TbMn_6Sn_6$ and YMn_6Sn_6

The intrinsic AHC can be calculated by integrating the Berry curvature over the Brillouin zone (BZ)[45]:

$$\sigma_{\alpha\beta} = -\frac{e^2}{\hbar}\int_{BZ}\frac{d\vec{k}}{(2\pi)^3}\sum_n f(E_{n\vec{k}})\Omega_n(\vec{k}) \quad (4)$$

where $f(E_{n\vec{k}})$ is the Fermi-Dirac distribution, $\Omega_{n,\alpha\beta}(\vec{k})$ is the contribution to the Berry curvature from state n, and $\alpha, \beta = \{x, y, z\}$.

A notable aspect of the calculation is the pronounced and rapid oscillation observed in the Berry curvature across the BZ, requiring a dense k mesh to ensure convergence. To accelerate the calculations, we implemented Eq. (4) in our recently-developed tight-binding (TB) code[46] and carried out the AHC calculations in RMn_6Sn_6 where R = Tb and Y. A realistic TB Hamiltonian was constructed using the maximally localized Wannier functions (MLWFs) method[47–49] implemented in WANNIER90[50] after the self-consistent density-functional-theory calculations performed using WIEN2K. A set of 118 Wannier functions (WFs) consisting of Y-4d (or Tb-5d), Mn-3d, and Sn-sp orbitals offers an effective representation of the electronic structure near the Fermi level (E_F). The self-consistent DFT calculations were carried out with out-of-plane magnetization in $TbMn_6Sn_6$ and both in- and out-of-plane magnetization in YMn_6Sn_6. For the in-plane YMn_6Sn_6 configuration, the moment is along lattice vector **a**, as denoted in Fig. 7. A dense 256^3 k-point mesh is used for the AHC calculations in TB.

Figure 7 presents the unit cell of YMn_6Sn_6 used in our calculation. The Cartesian coordinate system is chosen so that the lattice vector **b** is along the y-axis, **c** is along the z-axis, and **a** is along the −30° direction off the x-axis. Lattice vectors **a** and **b** point along the nearest neighboring (NN) Mn–Mn bond direction. For the σ_{xy} calculations discussed below, the first subscript x denotes the current direction, and the second subscript y denotes the Hall-field direction.

Figure 8 shows the AHC values calculated at $T = 0$= K as functions of Fermi energy using Eq. (4). In the out-of-plane orientation of both $TbMn_6Sn_6$ and YMn_6Sn_6, only σ_{xy} exhibits substantial values, while σ_{yz} and σ_{zx} remain negligible, as illustrated in the top and middle panels of Fig. 8. Conversely, with in-plane magnetization in YMn_6Sn_6, both σ_{yz} and σ_{zx} demonstrate appreciable values, while σ_{xy} remains negligible, as depicted in the bottom panel of Fig. 8. The band-filling calculation indicates that when doping YMn_6Sn_6 by 0.09 hole/Mn, corresponding to a Fermi energy shift of −0.037 eV, $\sigma_{xy} = 77.62$ S/cm, and $\sigma_{zx} = 36.76$ S/cm. While the former closely aligns with the experimental value, the latter is approximately 10 times smaller than the experiment. These comparison has to be taken

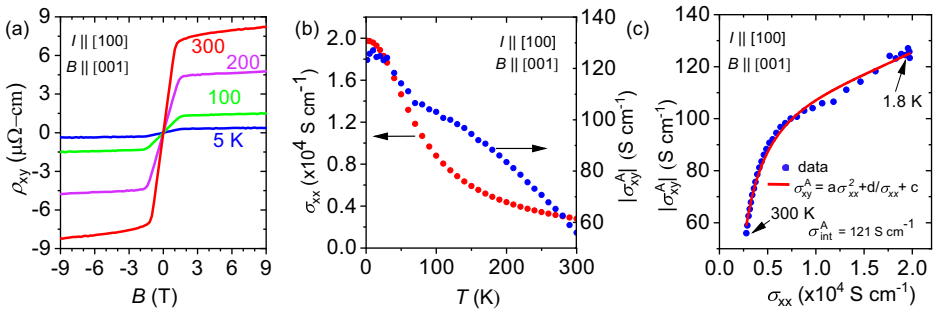

Fig. 5 | Anomalous Hall effect of $YMn_6Sn_{5.45}Ga_{0.55}$ measured with B|| [001] and I|| [100]. **a** Anomalous Hall resistivity ρ_{xy} as a function of magnetic field at selected temperatures. **b** Longitudinal conductivity (σ_{xx}, red spheres), and anomalous Hall conductivity ($|\sigma^A_{xy}|$, blue spheres) as a function of temperature. **c** $|\sigma^A_{xy}|$ (blue spheres) plotted as a function of σ_{xx} in the temperature range 1.8–300 K. The solid represents a fit to Eq. (2).

with caution, as random substitution of 0.55 Ga likely affects the electronic structure beyond a simple rigid Fermi energy shift. Nevertheless, our theoretical calculations predict that the Hall transport in *R*166 is 3D, consistent with the experimental findings.

We reported results of magnetic and electrical transport measurements of $YMn_6Sn_{5.45}Ga_{0.55}$ in two different geometries, supported by first-principles and DFT calculations. Our magneto-transport measurements across these two geometries confirm a more reliable scaling law that not only extracts the intrinsic AHC, but also accounts for contributions from spin fluctuations. These measurements revealed the 3D nature of the intrinsic AHC, which we attribute to the ferromagnetic properties of the material. The excellent agreement of the AHE with the empirical scaling law over the entire temperature suggests that this scaling relation may be important for not only for the large family of RMn_6Sn_6 ferro/ferrimagnetic compounds, but also for other systems with strong spin fluctuations.

Methods

Crystal growth and structural characterization

Single crystals of $YMn_6Sn_{5.45}Ga_{0.55}$ were grown by using Sn as a flux by the molten flux method. Y pieces (Alfa Aesar 99.9%), Mn pieces (Alfa Aesar 99.95%), Sn shots (Alfa Aesar 99.999%) and Ga pieces (Alfa Aesar 99.9999%) were added into a 2-mL aluminum oxide crucible in molar ratio of 1:6:18:2. The crucible was then sealed in a fused silica ampule under vacuum. The sealed ampule was heated to 1150 °C over 10 h, homogenized at 1150 °C for 24 h, and then cooled down to 600 °C with a rate of 5 °C/h. Once the furnace reached 600 °C, the molten flux was separated from the crystals by using a centrifuge. Upon opening the crucible, nice hexagonal-looking crystals up to 20 mg were obtained.

The crystal structure and the atomic composition were verified from a single crystal X-ray diffraction experiment. An arbitrary sphere of data was collected on a silver block-like crystal, having appropriate dimensions of 0.073 × 0.068 × 0.026, on a Bruker D8 diffractometer equipped with a Bruker APEX-II detector using a combination of ω- and ϕ-scans of 0.5°[51]. Data were corrected for absorption and polarization effects and analyzed for space group determination[52]. The structure was solved by dual-space methods and expanded routinely[53]. The model was refined by full-matrix least-squares analysis of F^2 against all reflections[54].

Table 3 | Comparison of intrinsic anomalous Hall conductivity between $TbMn_6Sn_6$[12] and $YMn_6Sn_{5.45}Ga_{0.55}$

Compound	*c* (S/cm)	*a* (S/cm)$^{-1}$	*d* (S/cm)^2
$TbMn_6Sn_6$ ($\lvert\sigma_{xy}\rvert$)	140	8.69×10^{-9}	-2.47×10^5
$YMn_6Sn_{5.45}Ga_{0.55}$ ($\lvert\sigma_{xy}\rvert$)	121	3.25×10^{-8}	-1.75×10^5
$YMn_6Sn_{5.45}Ga_{0.55}$ ($\lvert\sigma_{xz}\rvert$)	310	1.89×10^{-7}	-5.41×10^5

Magnetic property measurements

DC magnetization, resistivity, and magnetoresistance measurements were performed in a Quantum Design Dynacool Physical Property Measurement System (PPMS) with a 9 T magnet. ACMS II option was used in the same PPMS for DC magnetization measurements. Single crystals of $YMn_6Sn_{5.45}Ga_{0.55}$ were polished to adequate dimensions for electrical transport measurements. Crystals were oriented with the [001] and [100] directions parallel to the applied field for the c-axis and ab-plane measurements.

Resistivity and magnetotransport measurements

Resistivity and Hall measurements were done using the 4-probe method. Pt wires of 25 μm were used for electrical contacts with contact resistances <30 Ω. Contacts were affixed with Epotek H20E silver epoxy. An electric current of 4 mA was used for the electrical transport measurements.

The samples were polished to dimensions of ~1.00 × 0.40 × 0.15 mm, with the long axis oriented along either the [100], [120] or [001] crystallographic direction.

The longitudinal resistivity, ρ_{ii}, was calculated from the measured longitudinal resistance, R_{ii}, using the relation: $\rho_{ii} = R_{ii}A/l$, where $A = td$ is the cross-sectional area (t is the thickness, and d is the width of the sample), and l is the length of the sample between the two voltage contacts.

The Hall resistivity was calculated using the relation: $\rho_{ij} = R_{ij}t$, where $R_{ij} = V_i/I_j$ and t represent the measured Hall resistance and the sample thickness, respectively. Here, V_i is the transverse voltage developed along the i-direction in the presence of a magnetic field along k, with current I_j in the j-direction. The indices i, j, and k are mutually orthogonal, representing x, y, or z directions in different measurement geometries.

To account for the contact misalignment, the antisymmetric (Hall) and symmetric (magnetoresistance) contributions to the resistivity and Hall data, respectively were corrected using symmetrization and anti-symmetrization techniques as follows:

$$\rho_{ii} = \frac{\rho_{ii}(+B) + \rho_{ii}(-B)}{2}, \quad \rho_{ij} = \frac{\rho_{ij}(+B) - \rho_{ij}(-B)}{2}.$$

The longitudinal resistivity and Hall resistivity data were acquired in a four-loop sequence: the magnetic field B was swept from $+B_{max}$ to $-B_{max}$, and then back from $-B_{max}$ to $+B_{max}$. Symmetrization and antisymmetrization were applied to data obtained during B-field sweeps from $+B_{max}$ to 0 and from $-B_{max}$ to 0, as well as from 0 to $+B_{max}$ and from 0 to $-B_{max}$.

Hall conductivity for various directions was calculated using the following relations:

$$\sigma_{xy} = \frac{-\rho_{xy}}{\rho_{xx}^2}, \quad \sigma_{zx} = \frac{-\rho_{zx}}{\rho_{xx}\rho_{zz}}.$$

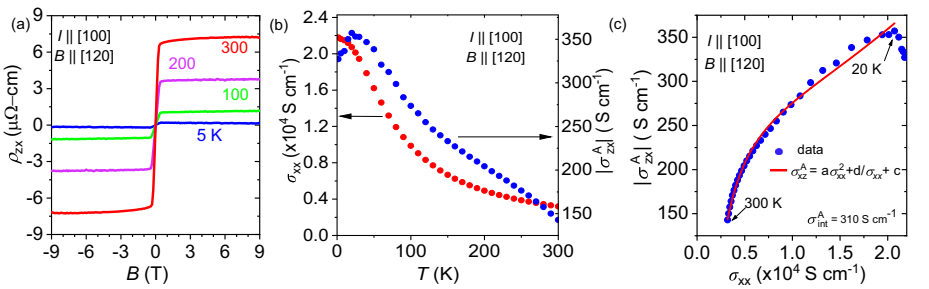

Fig. 6 | Anomalous Hall effect of $YMn_6Sn_{5.45}Ga_{0.55}$ measured with B|| [120] and I|| [100]. **a** Anomalous Hall resistivity ρ_{zx} as a function of magnetic field at selected temperatures. **b** Longitudinal conductivity (σ_{xx}, red spheres), and anomalous Hall conductivity ($|\sigma^A_{xz}|$, blue spheres) as a function of temperature. **c** $|\sigma^A_{zx}|$ (blue spheres) plotted as a function of σ_{xx} in the temperature range 1.8–300 K. The solid represents a fit to Eq. (2).

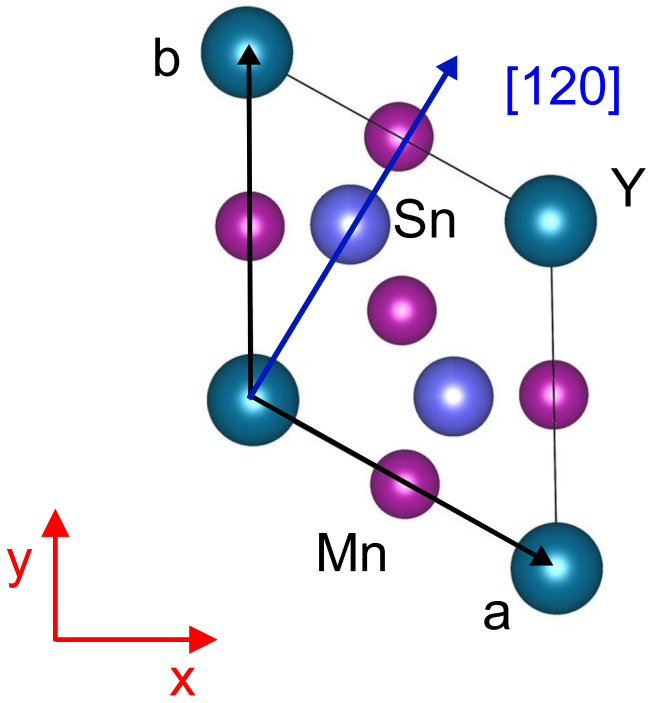

Fig. 7 | Primitive unit cell used in AHC calculations. The top view of the YMn_6Sn_6 primitive unit cell. The *x*- and *y*-axes are highlighted in red, while the [120] direction is denoted in blue. The *z*-axis is perpendicular to the plane.

Here, ρ_{xx}, and ρ_{zz} represent the longitudinal resistivities for current along the [100], and [001] crystallographic directions, respectively, with the magnetic field applied perpendicularly. For the calculation of σ_{yx}, both ρ_{xy} and ρ_{xx} were measured simultaneously in the same sample. For the calculation of σ_{zx}, ρ_{zx} and ρ_{xx} were measured simultaneously in the sample, and ρ_{zz} was measured on a separate crystal of the same growth batch. The term $\rho_{xx}\rho_{zz}$ in the denominator of σ_{xz} accounts for the resistivity anisotropy in the hexagonal system. For σ_{xy}, $\rho_{xx} = \rho_{yy}$ is used due to the isotropic in-plane resistivity. The conductivity relations used here are valid under the condition: $\rho_{ii}\rho_{jj} \gg \rho_{ij}\rho_{ji}$.

First-principles calculations

The first-principles calculations were performed using Vienna ab initio Simulation Package (VASP)[55] within projector augmented wave (PAW) method[56,57] The Perdew–Burke–Enzerhof (PBE)[58] generalized gradient approximation was employed to describe exchange-correlation effects. The on-site Coulomb interactions are taken into account using LDA + U[59] to improve the description of the interactions between localized 3*d*-electrons of Mn and an effective $U_{\text{eff}} = U - J = 0$, 0.6 and 2 are considered.

The experimental values were used for the lattice parameters and kept fixed for all the calculations, including the geometry optimization, where only internal coordinates were relaxed. To properly determine the structure, we performed geometry optimization for 2*d*, 2*e*, and 2*c* three different Ga substitution sites. The 2c site, consistent with the experimental analysis, gives the lowest energy which is then considered as the magnetic ground state.

Data availability

The authors declare that the main data supporting the findings of this study are available within the article. Extra data are available from the corresponding author upon request.

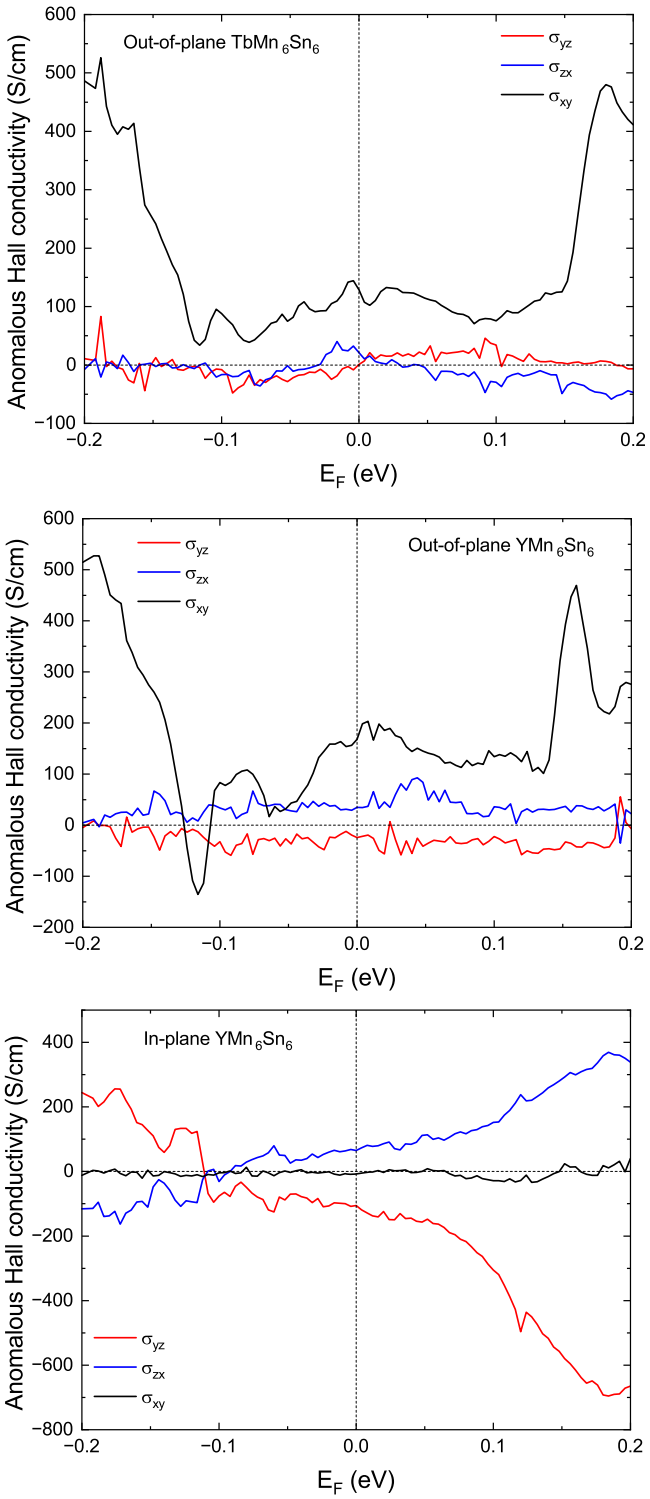

Fig. 8 | Calculated intrinsic anomalous Hall conductivity (AHC) of $TbMn_6Sn_6$ and YMn_6Sn_6 as a function of Fermi energy (E_F). The intrinsic AHC of $TbMn_6Sn_6$ (Top) was calculated with an out-of-plane magnetization configuration, while that of YMn_6Sn_6 was calculated with both out-of-plane magnetization (Middle) and in-plane magnetization configurations (Bottom).

Received: 9 March 2025; Accepted: 12 August 2025;
Published online: 26 September 2025

References

1. Zhang, Z.-Y. Quantum Hall effect in kagomé lattices under staggered magnetic field. *J. Phys.* **23**, 425801 (2011).
2. Ghimire, N. J. & Mazin, I. I. Topology and correlations on the kagome lattice. *Nat. Mater.* **19**, 137 (2020).
3. Kang, M. et al. Dirac fermions and flat bands in the ideal kagome metal FeSn. *Nat. Mater.* **19**, 163 (2020).
4. Ye, L. et al. Massive Dirac fermions in a ferromagnetic kagome metal. *Nature* **555**, 638 (2018).
5. Yin, J.-X. et al. Negative flat band magnetism in a spin–orbit-coupled correlated kagome magnet. *Nat. Phys.* **15**, 443 (2019).
6. Kuroda, K. et al. Evidence for magnetic Weyl fermions in a correlated metal. *Nat. Mater.* **16**, 1090 (2017).
7. Mazin, I. I. et al. Theoretical prediction of a strongly correlated Dirac metal. *Nat. Commun.* **5**, 4261 (2014).
8. Bolens, A. & Nagaosa, N. Topological states on the breathing kagome lattice. *Phys. Rev. B* **99**, 165141 (2019).
9. Asaba, T. et al. Anomalous Hall effect in the kagome ferrimagnet $GdMn_6Sn_6$. *Phys. Rev. B* **101**, 174415 (2020).
10. Bhandari, H. et al. Magnetism and fermiology of kagome magnet $YMn_6Sn_4Ge_2$. *npj Quantum Mater.* **9**, 6 (2024).
11. Pokharel, G. et al. Electronic properties of the topological kagome metals YV_6Sn_6 and GdV_6Sn_6. *Phys. Rev. B* **104**, 235139 (2021).
12. Jones, D. C. et al. Origin of spin reorientation and intrinsic anomalous Hall effect in the kagome ferrimagnet $TbMn_6Sn_6$. *Phys. Rev. B* **110**, 115134 (2024).
13. Pokharel, G. et al. Highly anisotropic magnetism in the vanadium-based kagome metal TbV_6Sn_6. *Phys. Rev. Mater.* **6**, 104202 (2022).
14. Arachchige, H. W. S. et al. Charge density wave in kagome lattice intermetallic ScV_6Sn_6. *Phys. Rev. Lett.* **129**, 216402 (2022).
15. Riberolles, S. et al. Orbital character of the spin-reorientation transition in $TbMn_6Sn_6$. *Nat. Commun.* **14**, 2658 (2023).
16. Lee, Y. et al. Interplay between magnetism and band topology in the kagome magnets RMn_6Sn_6. *Phys. Rev. B* **108**, 045132 (2023).
17. Ghimire, N. J. et al. Competing magnetic phases and fluctuation-driven scalar spin chirality in the kagome metal YMn_6Sn_6. *Sci. Adv.* **6**, eabe2680 (2020).
18. Wang, Q. et al. Field-induced topological Hall effect and double-fan spin structure with a c-axis component in the metallic kagome antiferromagnetic compound YMn_6Sn_6. *Phys. Rev. B* **103**, 014416 (2021).
19. Siegfried, P. E. et al. Magnetization-driven Lifshitz transition and charge-spin coupling in the kagome metal YMn_6Sn_6. *Commun. Phys.* **5**, 1 (2022).
20. Yin, J.-X. et al. Quantum-limit Chern topological magnetism in $TbMn_6Sn_6$. *Nature* **583**, 533 (2020).
21. Riberolles, S. et al. Low-Temperature Competing Magnetic Energy Scales in the Topological Ferrimagnet $TbMn_6Sn_6$. *Phys. Rev. X* **12**, 021043 (2022).
22. Mielke III, C. et al. Low-temperature magnetic crossover in the topological kagome magnet $TbMn_6Sn_6$. *Commun. Phys.* **5**, 107 (2022).
23. Li, Z. et al. Discovery of Topological Magnetic Textures near Room Temperature in Quantum Magnet $TbMn_6Sn_6$, Advanced Materials, 2211164 (2023).
24. Xu, X. et al. Topological charge-entropy scaling in kagome Chern magnet $TbMn_6Sn_6$. *Nat. Commun.* **13**, 1197 (2022).
25. Gao, L. et al. Anomalous Hall effect in ferrimagnetic metal RMn_6Sn_6 (R= Tb, Dy, Ho) with clean Mn kagome lattice. *Appl. Phys. Lett.* https://pubs.aip.org/aip/apl/article-abstract/119/9/092405/41513/Anomalous-Hall-effect-in-ferrimagnetic-metal?redirectedFrom=fulltext (2021).
26. Riberolles, S. X. et al. New insight into tuning magnetic phases of RMn_6Sn_6 kagome metals. *npj Quantum Mater.* **9**, 42 (2024).
27. Wenzel, M. et al. Effect of magnetism and phonons on localized carriers in the ferrimagnetic kagome metals $GdMn_6Sn_6$ and $TbMn_6Sn_6$. *Phys. Rev. B* **106**, L241108 (2022).
28. Okamura, Y. et al. Observation of anomalous Hall resonance of massive Dirac fermions in topological kagome-lattice magnet. *npj Quantum Mater.* **8**, 57 (2023).
29. Zhang, H. et al. Exchange-biased topological transverse thermoelectric effects in a Kagome ferrimagnet. *Nat. Commun.* **13**, 1091 (2022).
30. Crépieux, A. & Bruno, P. Theory of the anomalous Hall effect from the Kubo formula and the Dirac equation. *Phys. Rev. B* **64**, 014416 (2001).
31. Tian, Y., Ye, L. & Jin, X. Proper scaling of the anomalous Hall effect. *Phys. Rev. Lett.* **103**, 087206 (2009).
32. Yang, S. A., Pan, H., Yao, Y. & Niu, Q. Scattering universality classes of side jump in the anomalous Hall effect. *Phys. Rev. B* **83**, 125122 (2011).
33. Ishizuka, H. & Nagaosa, N. Large anomalous Hall effect and spin hall effect by spin-cluster scattering in the strong-coupling limit. *Phys. Rev. B* **103**, 235148 (2021).
34. Ishizuka, H. & Nagaosa, N. Spin chirality induced skew scattering and anomalous Hall effect in chiral magnets. *Sci. Adv.* **4**, eaap9962 (2018).
35. Neubauer, K. J. et al. Correlation between complex spin textures and the magnetocaloric and Hall effects in $Eu(Ga_{1-x}Al_x)_4$ (x= 0.9, 1). *Phys. Rev. B* **111**, 165136 (2025).
36. Grigoryan, V. L., Xiao, J., Wang, X. & Xia, K. Anomalous Hall effect scaling in ferromagnetic thin films. *Phys. Rev. B* **96**, 144426 (2017).
37. Xu, C., Heitmann, T., Zhang, H., Xu, X. & Ke, X. Magnetic phase transition, magnetoresistance, and anomalous Hall effect in Ga-substituted YMn_6Sn_6 with a ferromagnetic kagome lattice. *Phys. Rev. B* **104**, 024413 (2021).
38. Zhang, S.-y. et al. Magnetism and giant magnetoresistance of $YMn_6Sn_{6-x}Ga_x$ (x= 0-1.8) compounds. *Phys. Rev. B* **64**, 212404 (2001).
39. Dally, R. L. et al. Chiral properties of the zero-field spiral state and field-induced magnetic phases of the itinerant kagome metal YMn_6Sn_6. *Phys. Rev. B* **103**, 094413 (2021).
40. Idrissi, B. C. E., Venturini, G. & Malaman, B. Magnetic structures of $TbMn_6Sn_6$ and $HoMn_6Sn_6$ compounds from neutron diffraction study. *J. Less Common Met.* **175**, 143 (1991).
41. Rosenfeld, E. & Mushnikov, N. Double-flat-spiral magnetic structures: Theory and application to the RMn_6X_6 compounds. *Physica B* **403**, 1898 (2008).
42. Blaha, P., Schwarz, K., Madsen, G. K. H., Kvasnicka, D. & Luitz, J., WIEN2K (2002), ISBN 3-9501031-1-2.
43. Li, M. et al. Dirac cone, flat band and saddle point in kagome magnet YMn_6Sn_6. *Nat. Commun.* **12**, 1 (2021).
44. Kimura, S. et al. High-field magnetization of RMn_6Sn_6 compounds with R= Gd, Tb, Dy and Ho. *J. Alloy. Compd.* **408**, 169 (2006).
45. Wang, X., Yates, J. R., Souza, I. & Vanderbilt, D. Ab initio calculation of the anomalous Hall conductivity by Wannier interpolation. *Phys. Rev. B* **74**, 195118 (2006).
46. Ke, L. Intersublattice magnetocrystalline anisotropy using a realistic tight-binding method based on maximally localized Wannier functions. *Phys. Rev. B* **99**, 054418 (2019).
47. Marzari, N. & Vanderbilt, D. Maximally localized generalized Wannier functions for composite energy bands. *Phys. Rev. B* **56**, 12847 (1997).
48. Souza, I., Marzari, N. & Vanderbilt, D. Maximally localized Wannier functions for entangled energy bands. *Phys. Rev. B* **65**, 035109 (2001).
49. Marzari, N., Mostofi, A. A., Yates, J. R., Souza, I. & Vanderbilt, D. Maximally localized Wannier functions: theory and applications. *Rev. Mod. Phys.* **84**, 1419 (2012).
50. Mostofi, A. A. et al. An updated version of wannier90: a tool for obtaining maximally-localised Wannier functions. *Comput. Phys. Commun.* **185**, 2309 (2014).

51. Bruker AXS, APEX-4, Bruker AXS, Madison, Wisconsin, USA (2021).
52. Krause, L., Herbst-Irmer, R., Sheldrick, G. M. & Stalke, D. Comparison of silver and molybdenum microfocus X-ray sources for single-crystal structure determination. *J. Appl. Crystallogr.* **48**, 3 (2015).
53. Sheldrick, G. M. Shelxt–integrated space-group and crystal-structure determination. *Acta Crystallogr. Sect. A* **71**, 3 (2015).
54. Sheldrick, G. M. Crystal structure refinement with shelxl. *Acta Crystallogr. Sect. C* **71**, 3 (2015).
55. Kresse, G. & Furthmüller, J. Efficient iterative schemes for ab initio total-energy calculations using a plane-wave basis set. *Phys. Rev. B* **54**, 11169 (1996).
56. Blöchl, P. E. Projector augmented-wave method. *Phys. Rev. B* **50**, 17953 (1994).
57. Kresse, G. & Joubert, D. From ultrasoft pseudopotentials to the projector augmented-wave method. *Phys. Rev. B* **59**, 1758 (1999).
58. Perdew, J. P., Burke, K. & Ernzerhof, M. Generalized gradient approximation made simple. *Phys. Rev. Lett.* **77**, 3865 (1996).
59. Anisimov, V. I. & Gunnarsson, O. Density-functional calculation of effective Coulomb interactions in metals. *Phys. Rev. B* **43**, 7570 (1991).

Acknowledgements

N.J.G. and H.B. acknowledge the support from the NSF CAREER award DMR-2343536. I.I.M. acknowledges support from the NSF award DMR-2403804. The work at the Ames National Laboratory was supported by the U.S. Department of Energy (US DOE), Office of Basic Energy Sciences, Division of Materials Sciences and Engineering. Ames National Laboratory is operated for the US DOE by Iowa State University under Contract No. DE-AC02-07CH11358. Disclaimer: Certain commercial equipment, instruments, software or materials are identified in this paper in order to specify the experimental procedure adequately. Such identification is not intented to imply recommendation or endorsement by NIST, nor is it intended to imply that the materials or equipment identified are necessarily the best available for the purpose.

Author contributions

N.J.G. and H.B. conceived the idea and coordinated the project. H.B. grew single crystals. R.B.R. and M.E.G. helped in the crystal growth. H.B., A.G.O., and A.D. characterized the structural and chemical composition of the samples. H.B. performed magnetic and magnetotransport measurements. P.E.S. helped in some magnetotransport measurements. H.B. carried out the data analysis. I.I.M. and P.H.C contributed to the DFT calculations. Z.N. and L.K. contributed to the AHC calculations. H.B. and N.J.G. wrote the manuscript with inputs from I.I.M., and L.K. All authors contributed to the discussion of the results.

Competing interests

The authors declare no Competing Financial or Non-Financial Interests.

Additional information

Correspondence and requests for materials should be addressed to Hari Bhandari or Nirmal J. Ghimire.